AIAA 81-2450R

In-Flight Deflection Measurement of the HiMAT Aeroelastically Tailored Wing

V. Michael DeAngelis*
NASA Ames Research Center, Edwards, California

An electro-optical flight deflection measurement system was developed for NASA for use on the highly maneuverable aircraft technology (HiMAT) remotely piloted research vehicle (RPRV) to provide a means for evaluating the performance of the HiMAT's aeroelastically tailored composite wing and canard. A description of the flight deflection measurement system is presented from a user's viewpoint and includes the general method of operation, system capabilities and limitations, method of installation on the HiMAT vehicle, and calibration of targets. Also included is a general description of the HiMAT RPRV and its design goals. Preliminary flight deflection and bending moment data were obtained at Mach 0.8 and 0.9 and were extrapolated to the Mach 0.9 maneuver design condition for comparison to NASTRAN predictions and ground loads tests results. The preliminary flight test results tended to agree with the results obtained from the static ground loads tests; that is, that the NASTRAN model overpredicted the streamwise twist of the composite outer wing panel.

Introduction

THE aeroelastic tailoring of aircraft structures has emerged as a new technology from the continuing demand to improve airplane performance over the largest possible envelope, particularly in the transonic flight region. The advent of improved aerodynamic and structural analysis tools allows the designer to attempt to incorporate aeroelastic tailoring in the design of new aircraft. The F-8 supercritical wing airplane was the first airplane to which aeroelastic tailoring was applied. The "design to" wing coordinates defined the wing cruise shape at Mach 0.99 and an altitude of 40,000 ft in order to control the wing's upper surface shock strength and location. Thus the designer was required to predict the aeroelastic deformation of the wing at the design cruise condition and incorporate the deflections in the manufacturing jig. The advent of composite materials has potentially enhanced aeroelastic tailoring, as demonstrated by the design concept incorporated in the highly maneuverable aircraft technology (HiMAT) remotely piloted research vehicle (RPRV). By controlling the streamwise twist of both the wing and the canard through composite aeroelastic tailoring, the designer has attempted to optimize the performance of the HiMAT vehicle at the transonic design condition of Mach 0.9, an altitude of 25,000 ft, and a maneuver load factor of 8*g* with minimum adverse effect on cruise performance. Aeroelastic tailoring has become a requirement for optimizing airplane performance in the transonic flight region and will be a design consideration in future aircraft, such as the advanced fighter technology integration (AFTI) F-111 mission adaptive wing and the forward swept wing airplanes.

To evaluate both the HiMAT RPRV's performance and the design tools used for aeroelastic tailoring, the measurement of in-flight structural deformations was needed. An early method of measuring airplane deflections made use of cameras and film readers. To gain the required resolution, a 70-mm off-the-shelf motor-driven camera was used. However, because of its bulk and weight, this camera was not suited for use on the 0.44-scale HiMAT RPRV. With a design limit load factor of 12*g*, the inertia of the camera became a significant factor in the design of the camera mount. The need to measure the in-flight wing deflection of the HiMAT RPRV for evaluating structural and aerodynamic performance and the inadequacy of the photographic methods for this particular application led to a contract which ultimately resulted in the manufacture of a Grumman Aerospace Corporation developed concept for an electro-optical flight deflection measurement system (FDMS).

This paper defines the aeroelastic tailoring of the HiMAT wing and canard in terms of surface deflections; describes the electro-optical FDMS developed for use on the HiMAT RPRV in terms of general method of operation, capability, and limitations; describes the installation of the FDMS on the HiMAT RPRV, including an analytical representation of the target/receiver relationship; and compares preliminary measurements of flight wing deflections with predicted data and ground test results.

HiMAT General Description

The HiMAT remotely piloted research vehicle (Fig. 1) is a 0.44-scale model of a 17,000-lb fighter airplane. The 3055-lb RPRV has a wingspan of 15.6 ft and a length of 19.9 ft and was designed to be air launched from a B-52 airplane.

Composites comprise a large percentage of the HiMAT structure. The aeroelastically tailored lifting surfaces are the canard and the outer wing panel. The latter is spliced to the wing at the vertical tail boom at about 43% of the wing semispan. Both of these surfaces use matrix-dominated graphite-epoxy laminates for which very little laboratory data are available. A detailed documentation of the aeroelastically tailored outer wing and canard structure is contained in Ref. 1.

HiMAT Design Requirements

Aeroelastic tailoring was applied to the HiMAT lifting surfaces to attempt to optimize the transonic maneuver performance of the airplane while minimizing the adverse effect that the lifting surface maneuver shape would have on cruise performance or range. Figure 2 depicts the tailoring requirements for the HiMAT outer wing panel. The solid line represents the desired maneuver twist distribution for the outer wing panel. The dotted line represents the jig shape or

---

Presented as Paper 81-2450 at the AIAA/SETP/SFTE/SAE/ITEA/IEEE 1st Flight Testing Conference, Las Vegas, Nev., Nov. 11-13, 1981; submitted Dec. 10, 1981; revision received April 12, 1982.

*Aerospace Engineer, Dryden Flight Research Facility.

built-in twist distribution. The dashed line is the twist distribution resulting from deflecting the leading- and trailing-edge flaps to optimize the maneuver camber. The difference between the solid line and the dashed line is the aeroelastic twist distribution. For the HiMAT RPRV the aeroelastic twist distribution was maximized in order to minimize the built-in twist. Figure 3 presents the HiMAT contractor's assessment of the effects of outer wing panel twist on maneuver drag. Airplane incremental drag coefficient is plotted against wingtip twist angle for three different lift coefficients. The contractor's design goal was to optimize the twist for a range of lift coefficients from 1.0 to 1.2, but the measured twist from static ground tests in Ref. 1 is shown to be about 1 deg short of the design goal. However, the resulting performance degradation is expected to be small, particularly at the maneuver design point, which is Mach 0.9, an altitude of 25,000 ft, and a load factor of 8*g* or a lift coefficient of 1.0.

Flight Deflection Measurement System

The Dryden Flight Research Facility recognized that in-flight deflection measurements were needed to evaluate the design of the HiMAT aeroelastically tailored lifting surfaces. In-flight deflection measurements were made previously at Dryden on the YF-12 airplane, the F-8 supercritical wing airplane, and the KC-135 winglets airplane using passive targets and the off-the-shelf camera mentioned previously. Because of the small size of the HiMAT RPRV, however, this camera could not be mounted adequately on the airplane, and a new deflection measurement system was sought.

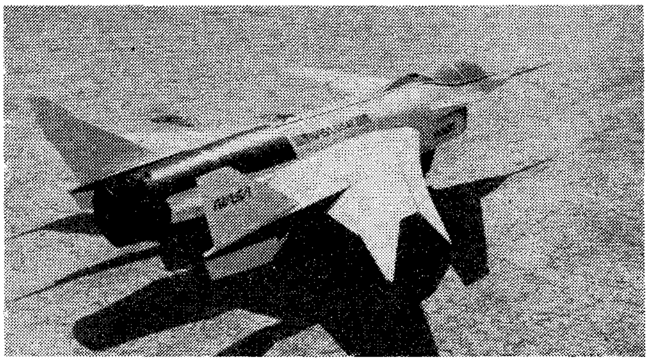

Fig. 1 HiMAT RPRV.

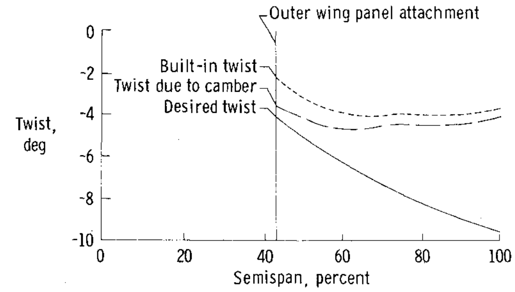

Fig. 2 HiMAT outer wing panel twist requirements; Mach 090, altitude = 25,000 ft, load factor = 8*g*.

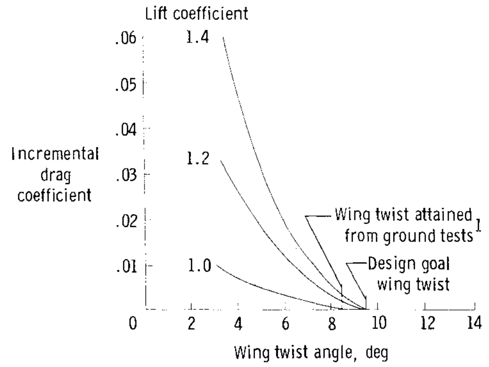

Fig. 3 Contractor's assessment of the effect of wingtip twist on incremental drag at Mach 0.90.

The major components of the resulting HiMAT FDMS (Fig. 4) are a control unit, two receivers, two target drivers, a ground display unit, and targets. The targets are infrared light-emitting diodes (LEDs) that are housed in aerodynamically shaped aluminum fixtures that are bonded to the airplane's structure. The FDMS was designed to operate up to 48 targets; however, for the HiMAT application the target drivers were built to accommodate eight targets each.

A system diagram for the HiMAT FDMS is shown in Fig. 5. The target LEDs are turned on and off sequentially, beginning with target 0 and ending with target 15. The sequencing through the 16 LED targets takes about 80 ms, at which time the sequence begins again with target 0, thus producing a sampling rate of 12.5 samples/s for each target. Light from the target LED passes through the cylindrical lens of the receiver and is focused as a line on a light-sensitive diode array that is mounted at the lens focal point. An electrical signal proportional to the point at which the target light encounters the diode array is relayed to the control unit by the receiver. The control unit, which contains the logic necessary to operate the FDMS, also serves to interface the FDMS with the PCM data recording system. The system is

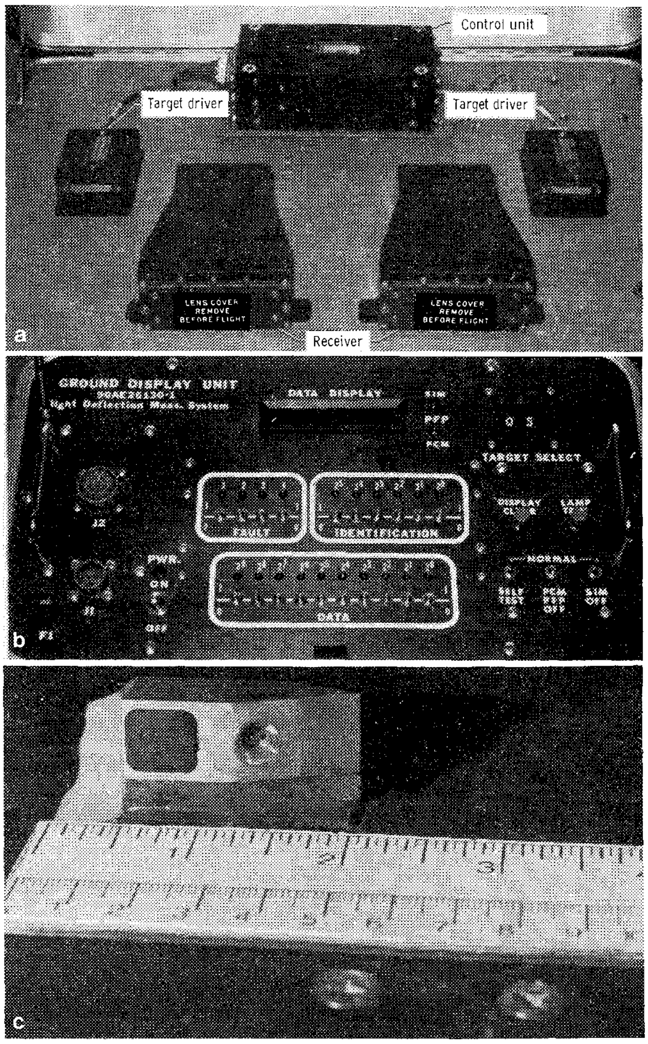

Fig. 4 FDMS components. a) Control unit, receiver, and target driver. b) Ground display unit. c) Target.

synchronized by using the PCM system end-of-frame pulse. Data are sent to the recording system as two 10-bit digital words. One word contains target identification and error messages. The other word contains the corresponding target position information. Once the data are acquired by the PCM system, the data are transmitted to a ground station for recording, displaying in real time, or both.

The ground display unit (Fig. 4b) provides for system synchronization in the absence of a PCM system by simulating the PCM end-of-frame pulse. In addition, the ground display unit decommutates the data word and displays target position data in decimal format.

Table 1 summarizes some of the general specifications of the HiMAT electro-optical FDMS and compares them to corresponding specifications for the photographic system previously used.

To make accurate in-flight deflection measurements, it is necessary not only to develop a good measurement system, but also to understand the operation of the system in its environment. Figure 6 depicts the geometric relationship between the FDMS receiver and a target. The reference coordinate system is a right-handed Cartesian coordinate system with the origin located at the center of the lens of the receiver and the x-y plane located parallel to the plane from which the deflections are measured. As shown in Fig. 6a, LP is the distance from the receiver to the target measured along the projection of the receiver centerline in the x-y plane. As shown in Fig. 6b, LP can be related to LD through trigonometric functions of β and ϕ. LD/Ld is the magnification of target T along the line TP'. However, target T moves along the line TP. At point P, the magnification becomes LD'/Ld. Therefore, except when $\beta = 0$ deg, the magnification changes with the position of the target.

The target position, Z, is defined as $Z = (\text{CAL})\ [(\text{Receiver output}) + (\text{Constant})]$, where CAL is the calibration factor and contains the magnification term. Without presenting a detailed derivation, the expression for the position of the target is

$$Z = \frac{(x\cos\alpha + y\sin\alpha)\ [KLd\tan\beta + (\text{CTS} - \text{CNTO})]}{[KLd - \tan\beta\ (\text{CTS} - \text{CNTO})]} \tag{1}$$

where CTS is the receiver output in counts; CNTO is the receiver output at receiver centerline in counts; Ld is the receiver focal length in inches; and K is the diode array scale factor, for this system 1000 counts/in.

As the above expression shows, the target position, Z, is a nonlinear function of the receiver output except when $\beta = 0$

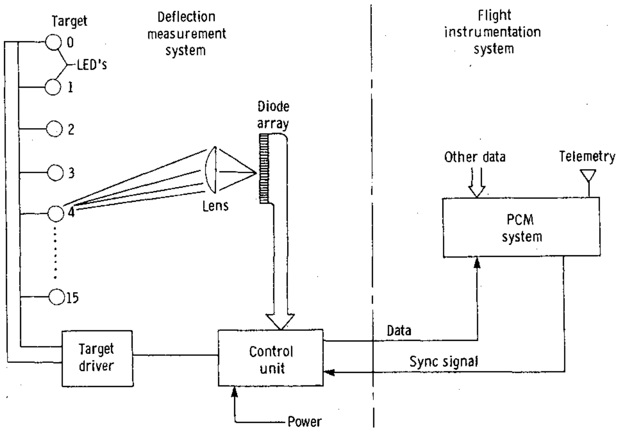

Fig. 5 System diagram for flight deflection measurement system.

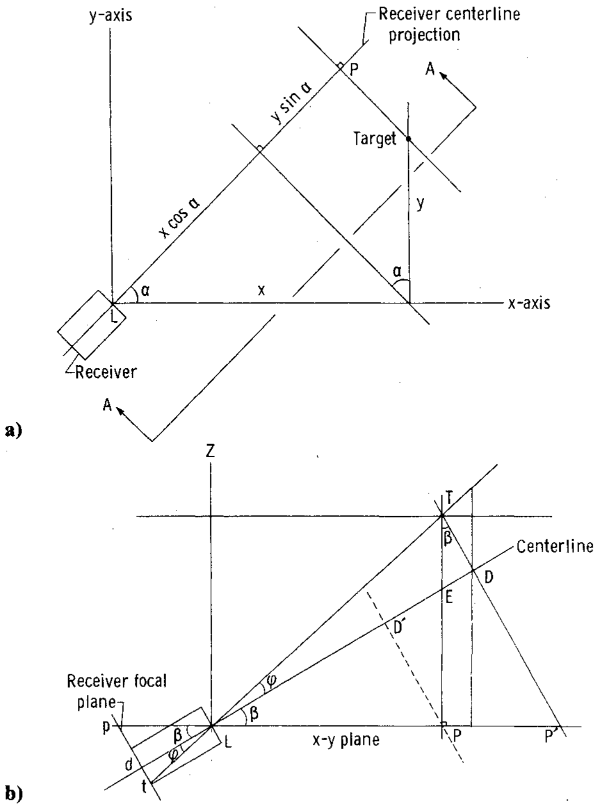

Fig. 6 Geometric relationship between the receiver and target. a) View looking down at x-y plane; $LP = x\cos\alpha + y\sin\alpha$. b) View A-A.

Table 1 General specifications of the photographic system used on the YF-12 airplane and the electro-optic system used on the HiMAT RPRV

	System	
	Photographic	Electro-optic
Camera/receiver		
Size, in.	8.5×4×5	6×6×2.5
Weight, lb	5	2.2
Field of view, deg		
Horizontal	50	30
Vertical	50	15
System		
Range, ft	>60	≅10
Resolution at 10 ft, in.	±0.11	±0.03
Target type	Passive	Active
Maximum number of targets	Unlimited	48
Maximum sampling rate, frames/s	1	200
Maximum amount of data acquired per flight	≅50 frames	Continuous
Flight environment	Mach 3	Mach 1.5

deg. The expression for Z can be written as follows:

$$Z = (\text{CAL})\,[KLd \tan\beta + (\text{CTS} - \text{CNTO})] \tag{2}$$

where

$$\text{CAL} = \frac{x\cos\alpha + y\sin\alpha}{KLd - \tan\beta(\text{CTS} - \text{CNTO})} \tag{3}$$

This puts the nonlinear receiver output term in the expression for the calibration factor. Measuring a displacement ΔZ based on a preflight reference value allows the expression for displacement to be written as follows:

$$\Delta Z_i = Z_i - Z_O = (\text{CAL})\,(\text{CTS}_i - \text{CTS}_O) \tag{4}$$

where the subscript O denotes a preflight or postflight reference value and the subscript i denotes any other value. However, this expression of ΔZ is not generally correct, since it is known that the value of CAL changes with receiver output except when $\beta = 0$ deg.

A discussion of the factors affecting the accuracy of the calibration of the system is beyond the scope of this paper. However, a brief discussion of the calibration approach used for the HiMAT application and an assessment of the accuracy of the HiMAT measurement system follows. First, it is necessary to describe the installation of the FDMS on the HiMAT RPRV (Fig 7). The power supply, control unit, and target drivers are mounted to the instrumentation pallet, which is located under the canopy. Two receivers are used; one measures wing deflections, while the other measures canard deflections. The wing receiver is mounted between the two main bulkheads of the HiMAT vehicle and therefore has a relatively rigid mount. Seven LED targets are attached to the wing. Targets 1-5 are epoxied to the upper surface of the wing; targets 6 and 7 are imbedded in the wingtip fillet. Photographs of the wing targets and of the faired wing receiver are presented in Figs. 8a and 8b. The canard receiver is mounted to the canopy, and four targets are epoxied to the upper surface of the canard. A discussion of the canard deflection measurements is not presented, because the canard data analysis is not complete.

Assuming that a linear relationship exists between the receiver output and the target deflection (when $\beta = 0$ deg), the value of CAL in Eq. (4) can be experimentally determined for each target. To perform the calibration, two LEDs were mounted on a bar 0.998 in. apart. The bar was then placed on the target perpendicular to the plane from which the target deflections were desired. Receiver outputs were recorded for the two calibration LEDs at each target location. CAL values, in inches per count, were then calculated from the equation

$$\text{CAL}_i = \left(\frac{0.998}{\text{CTS}_1 - \text{CTS}_2}\right)_i \tag{5}$$

where CTS_1 is the receiver output for one of the calibration LEDs; CTS_2 is the receiver output for the other calibration LED; and i is the target identification.

Since most applications of the FDMS require a β angle other than zero, an assessment of the error associated with using Eq. (5) to determine the CAL values is needed. Substituting the relationships $(\text{CTS} - \text{CNTO}) = KLd\tan\phi$ and $x\cos\alpha + y\sin\alpha = LP$ into Eq. (3) yields

$$\text{CAL} = \frac{LP}{KLd(1 - \tan\beta\tan\phi)} \tag{6}$$

where ϕ represents the vertical field of view angle of the receiver; LP is a measure of the distance from the target to the receiver; KLd is a term that remains constant for each receiver; and β is the receiver installation angle. The equation

$$\frac{\partial\text{CAL}/\partial\phi}{\text{CAL}} = \frac{\tan\beta}{\cos^2\phi(1 - \tan\beta\tan\phi)} \tag{7}$$

represents the percentage of error in the CAL value per radian change in ϕ with the assumption that the linear relationship expressed in Eq. (5) exists over the range of viewing angle, ϕ. Note that Eq. (7) is invariant with respect to receiver focal length and target position, but is a function of the receiver installation angle, β, which is -11 deg for the HiMAT wing receiver. Figure 9 presents Eq. (7) plotted against the receiver viewing angle, ϕ, for $\beta = 0$ and -11 deg. As the figure shows, the change in the calibration error with change in ϕ is very small for $\beta = -11$ deg and can be assumed to be 0.34%/deg over the entire range of ϕ. Of course, for $\beta = 0$ deg the calibration error becomes zero.

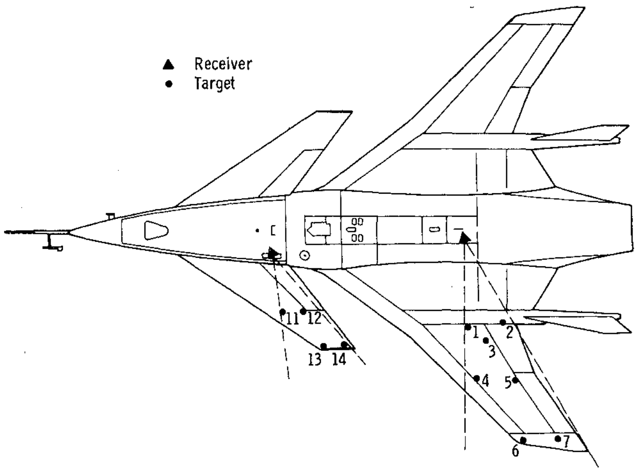

Fig. 7 HiMAT deflection measurement locations.

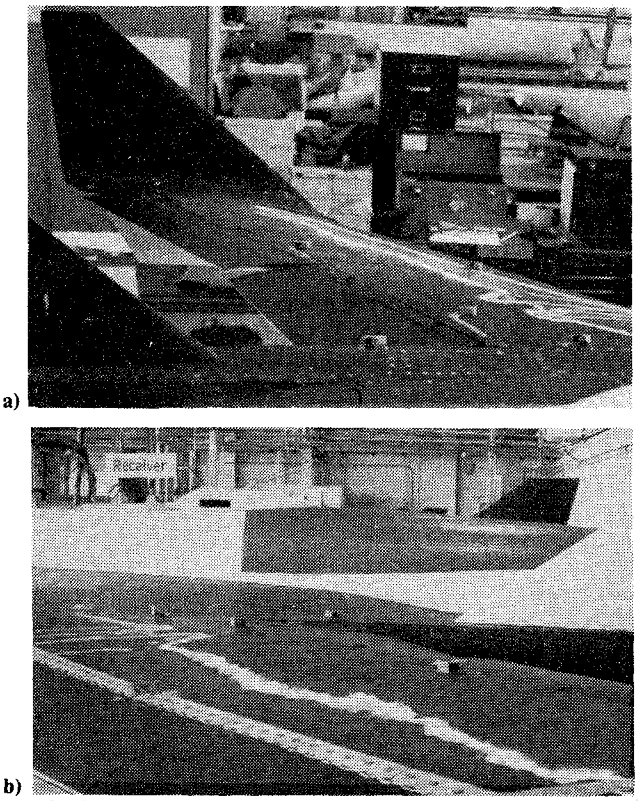

Fig. 8 FDMS wing receiver and targets on HiMAT. a) Targets on wing. b) Receiver.

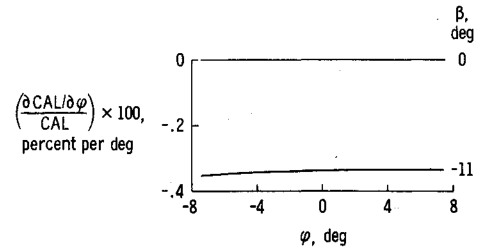

Fig. 9 CAL error associated with assuming a constant CAL value for all target positions.

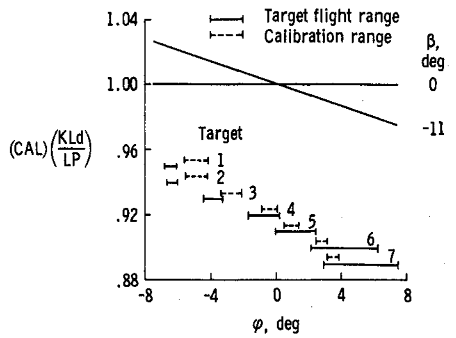

Fig. 10 Variation of normalized CAL with target position.

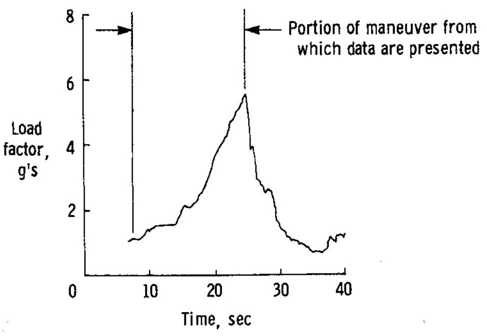

Fig. 11 Time history of windup-turn maneuver at Mach 0.9, altitude = 25,000 ft.

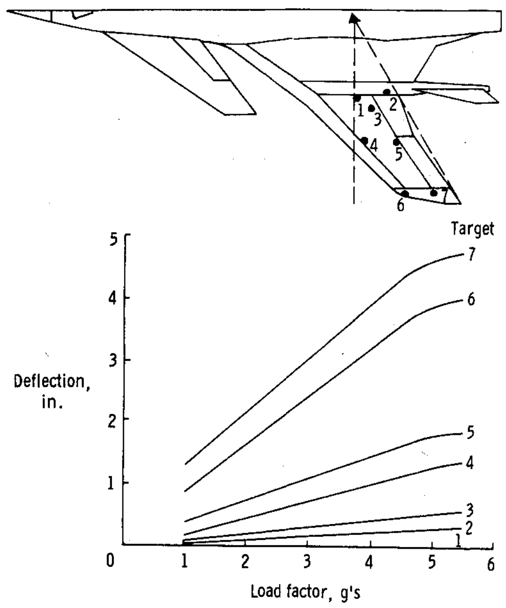

Fig. 12 Wing panel target deflection vs load factor at Mach 0.9, altitude = 25,000 ft. Data are preliminary.

To better understand the errors associated with assuming a linear CAL value and performing the target calibration as indicated by Eq. (5), it is necessary to modify the expression for CAL in Eq. (6). Multiplying both sides of the equation by KLd/LP produces

$$(\mathrm{CAL})\frac{KLd}{LP}=\frac{1}{1-\tan\beta\tan\phi} \tag{8}$$

The left side of the equation represents a target calibration that is normalized to receiver focal length and target position. As such, the normalized CAL is a function of receiver installation angle, β, and receiver vertical field of view angle, ϕ. The normalized CAL is plotted against ϕ for $\beta = 0$ and -11 deg in Fig. 10. The $\beta = -11$-deg curve depicts the variation of the CAL value over the vertical field of view of the receiver. This variation ranges from 0.975 to 1.026, or 5.1% of the ideal value of 1.0 when $\beta = 0$ deg. The solid brackets in the figure represent the range in ϕ that each target will traverse in order to measure the deflections associated with the HiMAT 8g design maneuver condition. The extreme left side of the bracket represents the target position when the wing is undeflected by airload (on the ground), while the extreme right side of the bracket represents the anticipated target position for the 8g design condition. The dashed brackets represent the ϕ range that results from conducting the linear calibration defined by Eq. (5) and used in Eq. (4). It is apparent from the figure that for targets closer to the receiver, the calibration range lies outside the target deflection range, and that for the farther targets, the target deflection range far exceeds the calibration range.

An error assessment assuming a constant CAL value for targets 1 and 7 follows. From Fig. 10, the CAL value for target 1 is established for a nominal ϕ of -4.9 deg. The target 1 ground zero ϕ is -6.8 deg, and the anticipated 8g ϕ is -6.0 deg, resulting in a nominal ϕ of -6.4 deg for the 8g target deflection. The CAL error associated with applying a CAL for $\phi = -4.9$ deg to data obtained at a ϕ of -6.4 deg is $[-4.9\ \mathrm{deg} - (-6.4\ \mathrm{deg})](-0.34)$, or -0.51%. This indicates that the CAL value is about 0.5% low for the range of the flight data. In terms of the 8g deflection, the error is 0.0026 in., which is about one-third the resolution error (± 0.009 in.) for target 1. The error for target 7 is 0.57%, or 0.043 in. The resolution error for target 7 is ± 0.024 in. These calibration errors can be reduced in several ways, one of which is to establish a nonlinear calibration curve for each target. Unfortunately, any method requires a significant increase in effort in data processing. Also, as β approaches 0 deg these errors approach zero, which requires that some forethought be given to the method of installation of the FDMS receiver.

Preliminary Flight Results

The electro-optical FDMS was operational for the first two airspeed calibration flights of the number 2 HiMAT vehicle. During the flight a 5.5g turn was flown at Mach 0.9 and a 6g turn was flown at Mach 0.8, both at an altitude of 25,000 ft. A time history of the Mach 0.9 maneuver including an indication of the portion of the maneuver from which data are presented is shown in Fig. 11.

Figure 12 presents deflections of the seven wing panel targets as a function of airplane normal acceleration for the maneuver presented in the previous figure. Targets 1-3 were installed in order to locate a reference plane at the root of the outer wing panel from which the deflections of targets 4-7 would be measured. Targets 4 and 5 are installed on the front and rear spars, respectively, to measure the streamwise twist at a midspan location on the outer wing panel, and targets 6 and 7 are located in such a way as to measure the wingtip streamwise twist. Above about 4g, the faired flight data show a nonlinear relationship with increasing load factor that is

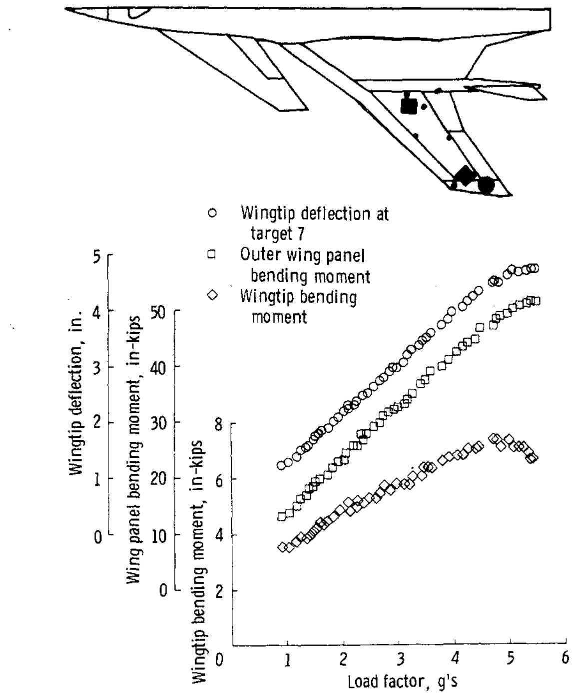

Fig. 13 Comparison of wingtip deflection and wing panel bending moment data. Data are preliminary.

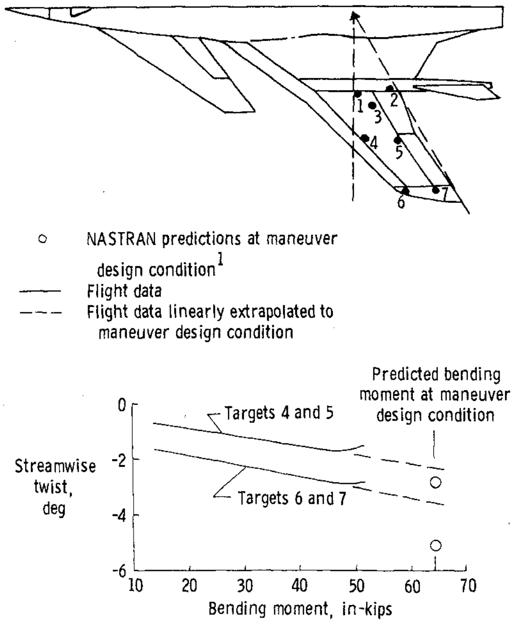

Fig. 14 Wing panel streamwise twist vs bending moment at Mach 0.9 and a comparison to predicted data. Flight data are preliminary.

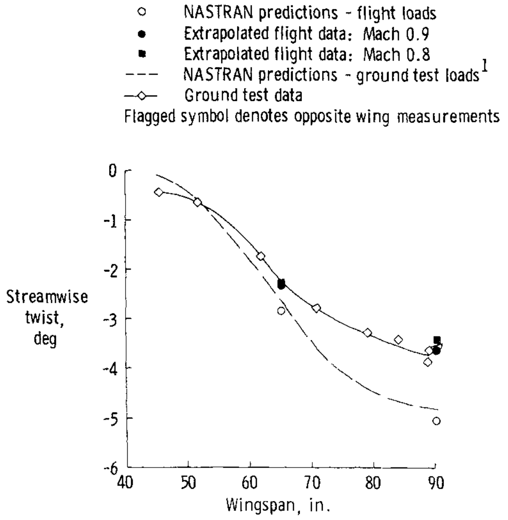

Fig. 15 Comparison of extrapolated flight test results to ground test data at the maneuver design point. Flight data are preliminary.

pronounced for the wingtip targets. The Mach 0.8 data show a similar nonlinearity above 3*g*. Restating again, the purpose of measuring the deflections of the wing is to provide data to evaluate the aeroelastically tailored wing panel at the maneuver design condition. The nature of the wingtip deflection data (the nonlinear behavior with increasing load factor) suggests that the aeroelastic twist may not attain the desired value at the 8*g* design condition. The remainder of this paper attempts a preliminary assessment of the aeroelastic performance of the outer wing panel at the maneuver design point.

Figure 13 presents a comparison of the wingtip deflection of target 7 to the outer wing panel root bending moment and the wingtip bending moment produced by the end plate. The root bending moment data and the deflection data show a similar trend with increasing load factor, whereas the tip bending moment data indicate a more severe loss of bending moment with increasing load factor to about 5*g*, at which point the bending moment begins to decrease. The data in this figure suggest that the nonlinear behavior of the deflection data results from a loss of load on the end plate.

Using load factor it is difficult to extrapolate the flight data for comparison to design point predictions because the flight data are for a different center of gravity location than that for the design point. However, using the wing panel root bending moment data affords a reasonable extrapolation, since only the relatively low torque loads are significantly different. The Mach 0.8 data can be handled in a similar way to provide supporting data. Figure 14 presents the midspan and wingtip streamwise twist as a function of wing panel bending moment. The linear extrapolation of the streamwise twist to the 8*g* predicted bending moment assumes that a linear deflection curve exists to that point. The limited data indicate that this might not occur. However, the linear extrapolation allows an assessment of the deflection or twist of the wing due to the predicted design bending moment. As shown by the data in the figure, the actual streamwise twist would fall short of that predicted by the NASTRAN model data in Ref. 1.

A comparison of the linearly extrapolated flight data and NASTRAN predictions for the maneuver design point with static ground test data from Ref. 1 is shown in Fig. 15. Data are presented for two different NASTRAN runs. The dashed curve represents NASTRAN predictions for the ground test loads, whereas the open circular symbols represent NASTRAN predictions for the flight loads. The preliminary flight test data tend to agree with the results of the ground tests; that is, that the NASTRAN model overpredicted the streamwise twist of the outer wing panel. However, it must be stressed that these flight data are preliminary and were obtained at flight conditions that do not exactly match the design condition.

Concluding Remarks

The advent of composite materials has potentially enhanced aeroelastic tailoring, as demonstrated by the design concept of the highly maneuverable aircraft technology (HiMAT) remotely piloted research vehicle. Aeroelastic tailoring was applied to the HiMAT lifting surfaces to attempt to optimize the transonic maneuver performance of the airplane while minimizing the adverse effect that the lifting surface maneuver shape would have on cruise performance.

To make in-flight deflection measurements of the HiMAT aeroelastically tailored surfaces, an electro-optical flight deflection measurement system (FDMS) was developed.

The general relationship between the target displacement (structural deflection) and the receiver output of the FDMS is nonlinear. However, with judicious planning of the installation of the system on the airplane, the nonlinear effects can be minimized.

The 5.5 and 6g windup-turn maneuvers were performed at Mach 0.9 and 0.8, respectively, both at an altitude of 25,000 ft. Preliminary wing panel deflection data and bending moment data suggest that at the higher load factors loss of load occurs on the end plate, resulting in a nonlinear wing deflection vs load factor curve.

To provide for a comparison between flight data and predictions, a linear extrapolation of the preliminary flight wing panel bending moment data to the 8g maneuver design condition at Mach 0.9 and an altitude of 25,000 ft was made. A comparison of the preliminary flight measured deflections to NASTRAN predictions tends to agree with the results of the static ground tests; that is, that the NASTRAN model overpredicted the streamwise twist of the outer wing panel.

Reference

[1] Monaghan, R.C., "Description of the HiMAT Tailored Composite Structure and Laboartory Measured Vehicle Shape Under Load," NASA TM 81354, 1981.

From the AIAA Progress in Astronautics and Aeronautics Series...

EXPERIMENTAL DIAGNOSTICS IN COMBUSTION OF SOLIDS—v. 63

Edited by Thomas L. Boggs, Naval Weapons Center, and Ben T. Zinn, Georgia Institute of Technology

The present volume was prepared as a sequel to Volume 53, *Experimental Diagnostics in Gas Phase Combustion Systems,* published in 1977. Its objective is similar to that of the gas phase combustion volume, namely, to assemble in one place a set of advanced expository treatments of diagnostic methods that have emerged in recent years in experimental combustion research in heterogenous systems and to analyze both the potentials and the shortcomings in ways that would suggest directions for future development. The emphasis in the first volume was on homogenous gas phase systems, usually the subject of idealized laboratory researches; the emphasis in the present volume is on heterogenous two- or more-phase systems typical of those encountered in practical combustors.

As remarked in the 1977 volume, the particular diagnostic methods selected for presentation were largely undeveloped a decade ago. However, these more powerful methods now make possible a deeper and much more detailed understanding of the complex processes in combustion than we had thought feasible at that time.

Like the previous one, this volume was planned as a means to disseminate the techniques hitherto known only to specialists to the much broader community of research scientists and development engineers in the combustion field. We believe that the articles and the selected references to the literature contained in the articles will prove useful and stimulating.

339 pp., 6×9, illus., including one four-color plate, $20.00 Mem., $35.00 List

TO ORDER WRITE: Publications Dept., AIAA, 1290 Avenue of the Americas, New York, N.Y. 10104